Downloaded from http://sp.lyellcollection.org/ by guest on March 27, 2020

The influence of clay content on submarine slope failure: insights from laboratory experiments and numerical models

M. M. W. Silver[1]* and B. Dugan[1,2]

[1]Hydrologic Science and Engineering Program, Colorado School of Mines, Golden, CO 80401, USA

[2]Department of Geophysics, Colorado School of Mines, Golden, CO 80401, USA

MMWS, 0000-0001-5093-6876; BD, 0000-0002-2555-6430

*Correspondence: mmsilver@mymail.mines.edu

Abstract: Submarine slope failures pose risks to coastlines because they can damage infrastructure and generate tsunamis. Passive margin slope failures represent the largest mass failures on Earth, yet we know little about their dynamics. While numerous studies characterize the lithology, structure, seismic attributes and geometry of failure deposits, we lack direct observations of failure evolution. Thus, we lack insight into the relationships between initial conditions, slope failure initiation and evolution, and final deposits. To investigate submarine slope failure dynamics in relation to initial conditions and to observe failure processes we performed physical experiments in a benchtop flume and produced numerical models. Submarine slope failures were induced under controlled pore pressure within sand–clay mixtures (0–5 wt% clay). Increased clay content corresponded to increased cohesion and pore pressure required for failure. Subsurface fractures and tensile cracks were only generated in experiments containing clay. Falling head tests showed a log-linear relation between hydraulic conductivity and clay content, which we used in our numerical models. Models of our experiments effectively simulate overpressure (pressure in excess of hydrostatic) and failure potential for (non)cohesive sediment mixtures. Overall our work shows the importance of clay in reducing permeability and increasing cohesion to create different failure modes due to overpressure.

Submarine slope failures along continental margins pose risks to coastal communities because they can damage infrastructure and generate tsunamis. Mass transport deposits, which are archives of slope failures, have been widely studied because they record slope failure events on passive, active and transform margins. Submarine slope failures can travel large distances at high speeds, even on low-angle (<2°) slopes (Hühnerbach and Masson 2004). A submarine slope failure initiated by the 2018 Palu, Indonesia earthquake (magnitude (M_L) 7.5) produced a tsunami that killed 1944 people (Muhari *et al.* 2018). The 2006 Java tsunami that claimed 600 lives is also thought to have been the product of an earthquake-triggered submarine slope failure (Fritz *et al.* 2007). The 1929 Grand Banks slope failure was triggered by a M_L 7.2 earthquake and transported 200 km^3 of mud and sand a distance of up to 1000 km (Fine *et al.* 2005). The mass failure severed 12 telegraph cables, and 28 people were killed from the produced tsunami (Fine *et al.* 2005). Although earthquake activity is low along the US Atlantic margin, the 1929 Grand Banks failure indicates that submarine slope failures in the region continue to occur, and thus are a potential hazard (ten Brink *et al.* 2014). Infrastructure along the US Atlantic margin presents a potential tsunami flooding/damage vulnerability in the form of densely populated areas, port facilities, industrial sites and ten coastal nuclear power plants (ten Brink *et al.* 2014).

Despite the risks associated with submarine slope failures on passive margins, little is known about their initiation and dynamics. Along active margins, frequent earthquakes prevent thick sediment accumulation and seismic shaking may strengthen sediment, decreasing failure potential and size (Sawyer and Devore 2015). Submarine slope failures on passive margins have longer recurrence intervals than on active margins, which facilitates thick sediment accumulation before failure and yields much larger failures (ten Brink *et al.* 2016). While numerous studies characterize slope failure deposits in terms of lithology, structure, seismic attributes, geometry and rheology (McAdoo *et al.* 2000; Gazioğlu *et al.* 2005; Locat *et al.* 2010; Dan *et al.* 2010; Lucchi *et al.* 2012; Idarraga-García and Vargas 2013), we lack direct observations of slope failure initiation

From: Georgiopoulou, A., Amy, L. A., Benetti, S., Chaytor, J. D., Clare, M. A., Gamboa, D., Haughton, P. D. W., Moernaut, J. and Mountjoy, J. J. (eds) 2020. *Subaqueous Mass Movements and their Consequences: Advances in Process Understanding, Monitoring and Hazard Assessments*. Geological Society, London, Special Publications, **500**, https://doi.org/10.1144/SP500-2019-186

© 2020 The Author(s). This is an Open Access article distributed under the terms of the Creative Commons Attribution License (http://creativecommons.org/licenses/by/4.0/). Published by The Geological Society of London.
Publishing disclaimer: www.geolsoc.org.uk/pub_ethics

Downloaded from http://sp.lyellcollection.org/ by guest on March 27, 2020

and evolution. As a result, there is limited insight into the relationship between initial conditions, preconditioning, slope failure initiation and failure behaviour.

In this paper, we expand the knowledge of submarine slope failure processes through a suite of physical laboratory experiments. We investigated failure mechanics and dynamics as influenced by pore pressure, cohesion and clay content in a benchtop flume in the Geomechanics Laboratory at the Colorado School of Mines and developed numerical models that quantify the observed processes. In order to establish a reproducible foundation for understanding pore pressure, cohesion and clay content effects on slope stability, high sand to clay ratios (0–5 wt% clay) were selected for our initial experiments. We focused on a mechanistic understanding of dynamic processes rather than a specific geological study area. This experimental and modelling approach builds upon previous experiments that looked at the role of yield strength to assess failure morphology (Sawyer *et al.* 2012) by investigating how pre-failure geometry, clay content and pore pressure affect slope failure dynamics, including sediment remobilization.

Methods

Flume experiments

Subaqueous slope failures were induced within the flume under controlled pore pressure boundary conditions with varied mixtures of commercially available fine-grained sand (sub-angular quartz; 87% SiO_2 $D_{50} = 195$ μm) and clay (dioctahedral smectite; 63% SiO_2 and 21% Al_2O_3; $D_{90} = 44$ μm) constrained to a constant pre-failure slope geometry (Fig. 1). A wedge-shaped geometry was selected which measured 30.3 cm long and 6.8 cm tall, with a top horizontal surface of 10.7 cm that ultimately tapered down to the base of the flume at an angle of 19.4° (Fig. 1). Experiments utilizing 2% clay used a slight variation of this geometry (wedge extended to 34.8 cm length with a top horizontal plane 15.2 cm long with unchanged height and slope).

Sand–clay mixtures (wt%) investigated were: (1) 100% fine-grained sand (FG sand); (2) 98% FG sand + 2% clay; (3) 96% FG sand + 4% clay; and (4) 95% FG sand + 5% clay. A minimum of three experiment runs were performed for each mixture. For sand–clay mixtures, sand and clay were gently mixed with a counter-top mechanical mixer for 5 min. Sediment (sand or sand–clay mixtures) was then poured into the flume and shaped with a template to provide a consistent geometry between experiments. The flume was filled with tap water through the effluent fitting until the flume water level reached a height *c.* 0.5 cm above the downstream weir (Fig. 1). The system was then left undisturbed until the water level over the sediment equilibrated with the water level in Reservoir 2 (R2; Fig. 1). The height of Reservoir 1 (R1) was adjusted to raise the water level of R2 without inducing slope failure. The flow control inlet valve was then opened by a quarter turn (*c.* 90°) and water was permitted to flow from R1 into R2, through the pebble layer and overlying wire mesh, and into the sand or sand–clay mixture.

Next R1 was raised to increase pore pressure at the pebble–sediment interface. The pressure was increased by raising R1 in 1 cm increments, with pauses of 3–5 min after each increase, until failure was observed. When slope failure occurred, the time of the event, the water levels in R2 before and after the event, and the geomorphological characteristics of the failure event were recorded.

Photogrammetry was utilized to assist experiment analyses. High-resolution photographs and videos were taken using two GoPro HERO7 Black cameras, capturing cross-section and overhead views of each experiment. Photogrammetry allowed for analysis of failure and deposit geomorphology.

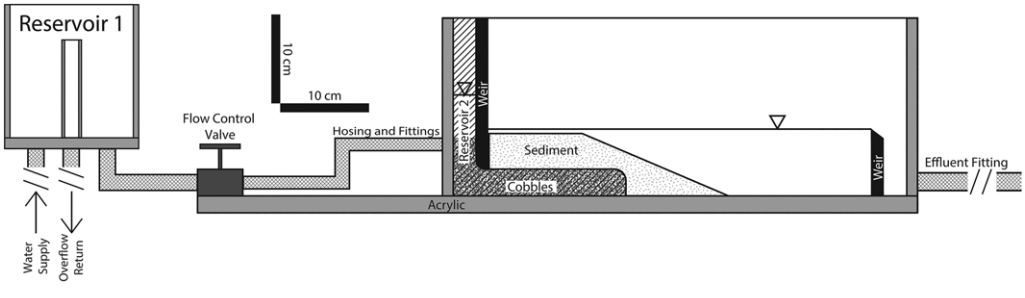

Fig. 1. Schematic diagram of the benchtop flume in the Geomechanics Laboratory at the Colorado School of Mines. The area labelled 'sediment' represents the typical experiment slope geometry. R2 is denoted with diagonal (45°) hatching.

Downloaded from http://sp.lyellcollection.org/ by guest on March 27, 2020

Permeability/hydraulic conductivity and porosity tests

Falling head tests were performed for each sediment mixture to constrain hydraulic conductivity. Sand–clay mixtures were prepared as previously described and arranged in triplicate as 12–13 cm long specimens (4 cm in diameter) in 25 cm long apparatuses. Tap water was chosen as the permeant to match our flume experiment conditions. Specimens were capped with a porous stone (*c.* 0.5 cm thick; top cap) and permeable membrane (base). Assemblies were submerged in water to depths sufficient to produce flow across the specimens and facilitate air removal and saturation (Berthila *et al.* 2010). Permeant liquid flowed from the base of the specimen upwards until the specimen was completely saturated. The specimen was then left in this state for a minimum of 24 h. The sample assemblies were then removed from the water and suspended, and water was added to the top of the specimens. The change in water level (head) over time was recorded to determine hydraulic conductivity (equation 1; Berthila *et al.* 2010). Falling-head experiments using prepared assemblies were run in triplicate (i.e. nine runs per sediment mixture).

$$K = \frac{\ln(h_1/h_2) \times L}{\Delta t} \tag{1}$$

where K is hydraulic conductivity (m s^{-1}), L is the length of the specimen (m), Δt is the interval of time (s) over which flow occurred, h_1 is head at t_1 (m) and h_2 is head at t_2 (m).

Sediment mixture bulk density was measured in triplicate and used to determine porosity to inform numerical modelling (equation 2; Fetter 2001),

$$n = 100\left(1 - \frac{\rho_b}{\rho_s}\right) \tag{2}$$

where n is porosity (%), ρ_b is bulk density (g cm^{-3}) and ρ_s is the density of dry solids (g cm^{-3}).

Numerical modelling

To quantify the experimentally observed failure processes, we developed groundwater flow models that simulated transient fluid flow through the experimental system and performed simple stability calculations based on the infinite slope approximation as a first-order characterization for how changes in overpressure, or pressure in excess of hydrostatic, correlate with locations of failure in our experimental set-up. Groundwater flow modelling used a simplified version of the groundwater flow equation,

$$\frac{S_s}{K}\frac{\partial h}{\partial t} = \frac{\partial^2 h}{\partial x^2} + \frac{\partial^2 h}{\partial y^2} \tag{3}$$

where S_s is the specific storage and h is the head. We assumed that all sediments are isotropic and that S_s was 0.981 m^{-1}. For the pebbles, we assumed a hydraulic conductivity of 9.81×10^{-2} m s^{-1}. For the sand and sand–clay mixtures, we used the average hydraulic conductivity values from the falling head experiments.

We used the spatially and temporally varying head data from the fluid flow models to estimate local stability based on an infinite slope factor of safety (FS) analysis,

$$FS = \frac{c + (\sigma'_{vh}\cos^2\theta - \rho g h^*)\tan\phi_f}{\sigma'_{vh}\cos\theta\sin\theta} \tag{4}$$

where c is cohesion, σ'_{vh} is the vertical effective stress assuming hydrostatic conditions, g, is acceleration due to gravity, h^*, is the head above hydrostatic conditions, θ is the seafloor slope (assumed constant and equal to 19°, similar to that of the flume experiments) and ϕ_f is the internal angle of friction. For cohesion, we assumed 10 Pa for every wt% clay (e.g. 4% clay equates to 40 Pa cohesion). This assumption allowed us to investigate how failure initiates and evolves with low values of cohesion that increase slightly with clay content. These values are within the range of cohesion for sand–clay mixtures based on the Unified Soil Classification System. For friction angle we assume 35° for 100% FG sand and decreased friction angle by 0.1° for each wt% clay added (e.g. 4% clay equates to ϕ_f of 34.6°). This approach provides a first-order estimate of where failure might occur and allows us to relate observed failures to fluid flow processes.

Results

Flume experiments

Slope failures initiated after sufficient water pressure was supplied through R2 and the pressure front migrated into the sediment above the pebbles. The water level within R2 required to initiate slope failure was 9.2 $\pm$ 0.2 cm ($\pm$1 SD) in sediment consisting of 100% FG sand (0% clay), 11.0 $\pm$ 0.4 cm in 98 wt% FG sand + 2 wt% clay, 11.5 $\pm$ 0.1 cm in 96% FG sand + 4% clay, and 12.2 $\pm$ 0.4 cm in 95% FG sand + 5% clay (Table 1). In seven experiments, we documented a decrease in the water level in R2 after a slope failure initiation; these systems then equilibrated at steady state. These steady-state R2 water levels increased with clay content from

Downloaded from http://sp.lyellcollection.org/ by guest on March 27, 2020

Table 1. *Water levels in R2 during experiments (in cm ± 1 SD) as a function of clay and FG sand content*

Sediment composition (wt%)	R2 water level prior to slope failure (cm)	Stable R2 water level following slope failure (cm)	Number of data points
100% FG sand	9.2 ± 0.2	9.2 ± 0.2	3
98% FG sand + 2% smectite (clay)	11.0 ± 0.4	10.6 ± 0.7	3
96% FG sand + 4% smectite (clay)	11.5 ± 0.1	10.9 ± 0	2
95% FG sand + 5% smectite (clay)	12.2 ± 0.4	8.9 ± 0.01	2

Column 3 presents steady-state R2 water level following slope failure initiation. The water level in R2 reached equilibrium with the water level within the experiment section once the influent valve was closed.

9.2 ± 0.2 cm (0% clay) to 10.9 ± 0 cm (4% clay) but decreased to their lowest point in 5% clay experiments (8.9 ± 0.01 cm; Table 1).

Geomorphic characteristics of slope failures varied with clay content. All experiments displayed some form of surficial eruption involving localized, vertical displacement of sediments ('sand volcanoes' Table 2; Fig. 2). Extensional surface cracking and suspension of clay particles was observed in all experiments involving clay. In experiments that had extensional surface cracking and surficial eruptions, extensional cracks were observed before surficial eruptions. Formation of elongated subsurface fissures along the flume–wall interface ('sidewall subsurface piping/fissures') was observed in one out of three of the 2% clay experiments, two out of three of the 4% clay experiments and all of the 5% clay experiments. Formation of subsurface fissures was observed after the formation of extensional cracking, but prior to surficial eruption. Each experiment resulted in downslope sediment transport, including but not limited to suspension of clay particles. No massive, blocky failures were observed.

Hydraulic conductivity and porosity

The hydraulic conductivity of sediment consisting of 100 wt% FG sand was $1.7 \times 10^{-4} \pm 1.6 \times 10^{-5}$ m s^{-1} (±1 SD); 98% FG sand + 2% clay was $5.4 \times 10^{-7} \pm 2.3 \times 10^{-7}$ m s^{-1}; 96% FG sand + 4% clay was 9.9×10^{-9} m s^{-1} $\pm 2.3 \times 10^{-9}$ m s^{-1}; and 95% FG sand + 5% clay was $7.8 \times 10^{-9} \pm 3.9 \times 10^{-9}$ m s^{-1}.

A best-fit linear regression was performed on $\log_{10}$ (hydraulic conductivity) as a function of clay content data for 40 experimental data points (Fig. 3). The regression from 0 to 5% clay yielded ($R^2 = 0.94$)

$$\log_{10}(K) = -0.8784cc - 4.1366 \qquad (5)$$

where *cc* is clay content (fraction; i.e. 5 wt% = 0.05). Extrapolation of this regression to clay concentrations exceeding 5 wt%, or mixtures not comparable to those described here, should be verified with additional experiments.

The porosity of 100 wt% FG sand was 47.2 ± 0.7% (±1 SD); 98% FG sand + 2% clay was 46.7 ± 1.9%; 96% FG sand + 4% clay was 49.0 ± 1.6%; and 95% FG sand + 5% clay was 48.7 ± 1.9%.

Numerical modelling

Numerical simulations quantified the fluid flow, overpressure and failure potential for our flume

Table 2. *Geomorphology of slope failures as a function of clay and FG sand content*

Sediment composition (wt%)	Surface eruption	Sidewall subsurface piping/fissures	Tension cracks	Suspension of clay particles	Downslope sediment transport
100% FG sand	3/3	0/3	0/3	N/A	3/3
98% FG sand + 2% smectite (clay)	3/3	1/3	3/3	3/3	3/3
96% FG sand + 4% smectite (clay)	3/3	2/3	3/3	3/3	3/3
95% FG sand + 5% smectite (clay)	2/2	2/2	2/2	2/2	2/2
Example photo figures	2a & 2b	2b	2a	2b	2b

Experiments that had slope failures unexpectedly during experiment set-up were excluded.

Downloaded from http://sp.lyellcollection.org/ by guest on March 27, 2020

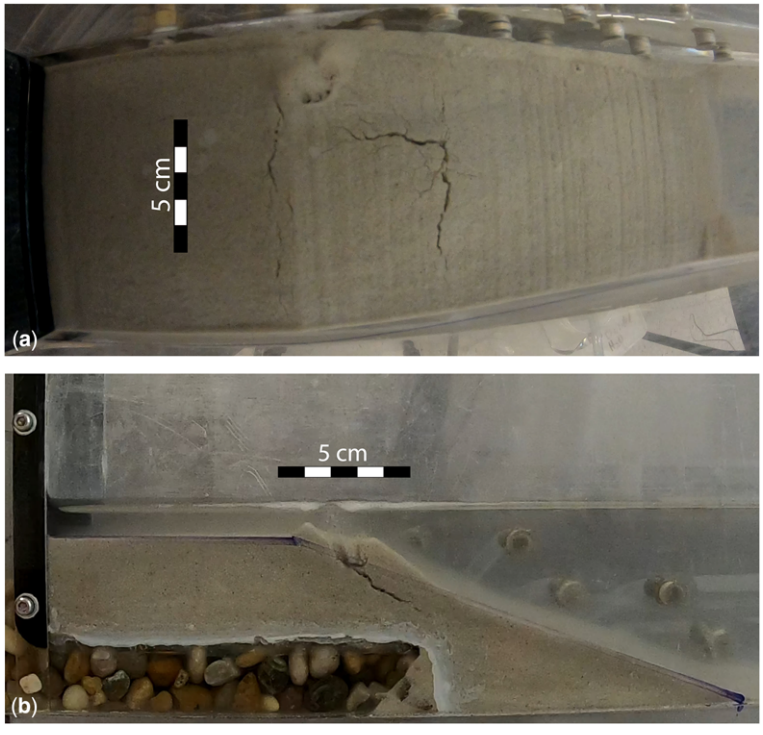

Fig. 2. (**a**) Overhead view of 4% clay experiment 2 showing four clustered sand volcanoes and extensional cracking. Surficial extensional cracking permitted focused water discharge. (**b**) Cross-section view of 4% clay experiment 3 displaying a sand volcano, subsurface piping/fissure, suspension of sediment particles and downslope sediment transport. Note: (a) and (b) are not to the same scale.

experiments. While our models are transient, we present results once the overpressure has equilibrated in the pebble layer, which allows us to determine failure potential when the entire high permeability zone is at its maximum overpressure. The numerical model of the 100% FG sand system documents a rapid (order of seconds) propagation of the overpressure from R2 through the sand. The maximum overpressure (pressure in excess of hydrostatic) at this point is 128 Pa in the pebble layer (Fig. 4a). The overlying sediment has low overpressure. The stability analysis predicts FS = 1 near the top of the sand (Fig. 4a). This is consistent with experimentally observed sand volcanoes at the surface of the sand (Table 2).

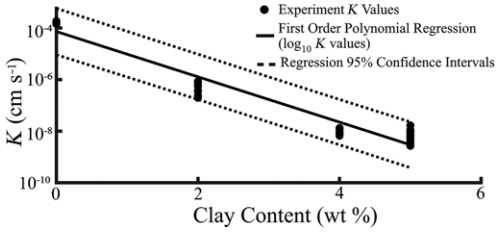

Fig. 3. Hydraulic conductivity as a function of clay determined by falling head method.

The numerical model of the 98% FG sand system documents a slower propagation (order of hundreds of seconds) of the overpressure from R2 into the sand–clay mixture. The maximum overpressure is 304 Pa in the pebble layer (Fig. 4b). The overlying sediment has moderate-to-low overpressure. The stability analysis predicts FS = 1 near the top of the sand–clay mixture and near the upper boundary of the pebble layer (Fig. 4b). This is consistent with experimentally observed sand volcanoes at the surface and fissures and cracks within the sand layer (Table 2).

The numerical models of the 96% FG sand and 95% FG sand are similar and document an even slower propagation (order of thousands of seconds) of the overpressure from R2 into the sand–clay mixture. The maximum overpressure is 372 Pa in the pebble layer of the 96% FG sand system (Fig. 4c) and is 442 Pa in the pebble layer of the 95% FG sand system (Fig. 4d). The stability analysis predicts

Downloaded from http://sp.lyellcollection.org/ by guest on March 27, 2020

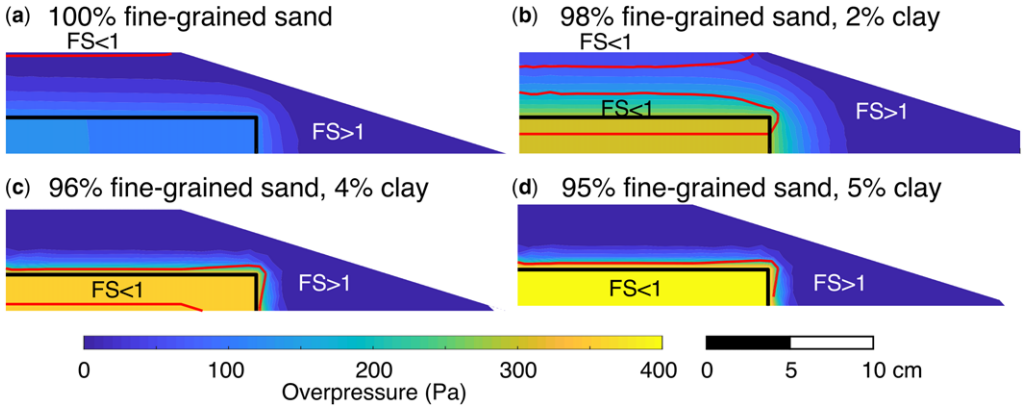

Fig. 4. Example results from numerical model of fluid flow and slope stability analysis for our flume experiments. For all plots, overpressure (or pressure in excess of hydrostatic) data are colour contoured at the same level (0–400 Pa), the thick red line is the factor of safety (FS) value of 1, and the thick black line is the boundary between the pebbles and the sediment (sand or sand–clay mixture). Zones where FS<1 and where FS>1 are labelled to show zones of instability (FS<1) and stability (FS>1). (**a**) Overpressure in the model of the 100% fine-grained (FG) sand experiment 1 s after raising the head in R2 to 9.2 cm. Maximum overpressure is 128 Pa. FS = 1 contour is localized near the top of the sediment between horizontal distance 0 and 10.5 cm, indicating that failure could initiate anywhere near the surface above that FS contour. (**b**) Overpressure in the model of the 2% clay experiment 500 s after raising the head in R2 to 11.0 cm. Maximum overpressure is 304 Pa. Two FS = 1 contours exist; one encompasses the boundary between the pebble layer and the sand–clay layer and extends to a horizontal distance of 16 cm and one is near the top of the sand–clay layer. This indicates that failure could initiate anywhere near the boundary of the pebble layer and the sand–clay layer or near the top of the sand–clay layer. Note: this model used a geometry based on the slightly different sediment geometry used in the 2% clay flume experiment. (**c**) Overpressure in the model of the 4% clay experiment 2500 s after raising the head in R2 to 11.5 cm. Maximum overpressure is 374 Pa. FS = 1 contour is near the base of the pebble layer and just above the pebble layer in the sand–clay layer, indicating that failure could initiate anywhere near the boundary of the pebble layer and the sand–clay layer. (**d**) Overpressure in the model of the 5% clay experiment 2500 s after raising the head in R2 to 11.5 cm. Maximum overpressure is 442 Pa. FS = 1 contour is in the sand–clay mixture parallel to the pebble layer, indicating that failure could initiate anywhere near the boundary of the pebble layer and the sand–clay layer. There is no vertical exaggeration.

FS = 1 near the boundaries of the pebble layer (Fig. 4c, d). This is consistent with experimentally observed sand volcanoes at the surface and fissures and cracks within the sand layer (Table 2).

Discussion

The water level of R2 controlled the slope failure, with increased R2 water levels prior to slope failure initiation directly correlating with increasing clay content (Table 1). As sand is non-cohesive and clay is cohesive, we interpret the increased cohesion with increasing clay content as increased resistance to failure. Decreases in R2 water levels immediately after slope failure initiation were likely a result of focused fluid flow through high permeability conduits produced by the failure. This was directly observed in cases where surface eruptions or subsurface fissures were produced in contact with the flume sidewall (e.g. Fig. 2b). The R2 water levels post-failure in relation to the water level within the flume experiment section may reflect differences in overall system permeability facilitated by differing scales of channellization following slope failure.

The lack of observed subsurface sidewall fissure formation and tensile cracking in sediment slopes of 100% FG sand indicated the importance of clay in their formation. We believe that clay particle size decreased permeability (Fig. 3), allowing the build-up of the higher pore pressures required to overcome the clay particle cohesive forces allowing failure. Once pore pressures exceeded the value to create failure, a subsurface fissure formed rapidly. Surficial extensional cracking was interpreted to be the result of sediment expansion produced by increasing pore pressure (Terzaghi *et al.* 1996). We note that subsurface sidewall fissures were present in experiments that contained clay (Table 2; Fig. 2b), but were not the origin of the failures. In many cases, these failures initiated within the sedimentary wedge and migrated to the sidewall. In addition, early deformation in the experiments included tension cracks on the surface that were not associated with sidewalls (Fig. 2a). Based on these observations, we surmise that these types of failures were

Downloaded from http://sp.lyellcollection.org/ by guest on March 27, 2020

controlled by water–sediment interactions and were not influenced by boundary effects (e.g. fluid migration along the sidewall).

Suspension of clay particles was anticipated for experiments involving sand–clay mixtures and is indicative of an active flow system where fluid expulsion resulted in the winnowing of clay particles. In most cases, the violent nature of slope failure initiation (surface eruption or sidewall piping) was enough to suspend clay particles within the top *c.* 1.5 cm of the flume experiment water column. Once suspended, clay particles travelled downslope due to gravity (towards the downstream weir) and remained in suspension for 12–24 h.

Slump failures, here defined as any cohesive, blocky failure or sedimentary folding, were not observed in any successful experiments. In some experiments, slumping was witnessed during experiment set-up, but this was prior to full saturation or total slope submergence. These experiments were ended and discredited as failed preparations, and they did not reflect the failure of a subaqueous slope under controlled pore pressure conditions. The lack of slumps in experiments may be the result of insufficient clay content (e.g. Sawyer *et al.* 2012) within the sediment and/or pore pressure being the only failure-inducing mechanism. Increased clay content is expected to increase cohesion within the slope and may allow for cohesive blocks of material to fail, rather than the observed channellization. The angle of the experiment slope was also considered as a potential cause of the lack of slumping. However, in natural marine environments, slump-like failures have been documented on slopes as low as 2° (Hühnerbach and Masson 2004). We therefore do not think the angle of our experiment slope (*c.* 19°) is the cause of this trend. A third effect that may increase slump-like behaviour is the rate of applied perturbations (e.g. pore pressure), which we did not explore in these experiments.

The sand volcano and tension crack geomorphological features observed in experiments resemble features observed in environments with greater clay content. For example, mud volcanoes have been observed in clay- and silt-dominated environments, such as the accretionary wedge offshore Costa Rica consisting of a carbonate-rich section overlain by hemipelagic sediment (clay- and silt-dominated; Shipley *et al.* 1990) or seaward of the Barbados accretionary complex (Westbrook and Smith 1983). Dam-break experiments performed by Sawyer *et al.* (2012), using mixtures of kaolin clay and silica silt, show fracture features in their source area resembling our observed experimental extensional crack features.

Surface eruption was the final stage of slope failure observed in all experiments. Formation of surficial extension cracks and subsurface cavities prior to surficial eruption was observed in some experiments. The observation of surface eruption as the most severe form of slope failure, combined with a lack of failure features post-eruption, indicates that eruption decreased excess pore pressure and increased local permeability, establishing a new stable system. Our documentation of progressive failure processes provides new insights into the temporal evolution of the final slope failure deposits.

Our numerical models correlate well with the general observations from our flume experiments. The models show that the decrease in permeability from the addition of clay impacts on the magnitude and distribution of the overpressure field (Fig. 4). This change in the overpressure field produces a change in the locus of failure (Fig. 4), with higher permeability, non-cohesive systems favouring shallow failure through surface eruption and lower permeability, cohesive systems evolving to deeper and more brittle failure modes (Table 2). In pure FG sand experiments, there were no failure processes or geomorphological features observed, suggesting deep sourcing for surface eruption. Clay experiments, however, displayed clear evidence for deeper sourcing for surface eruptions; in some instances, the source could be directly observed to extend to the pebble boundary. We interpret this to mean that small amounts of clay provide a decrease in permeability and cohesion that creates a change in the failure mode and the depth at which failure initiates.

While the qualitative link between our numerical models and physical experiments gives us confidence in understanding the basic processes and dynamics, our models do not provide exact replicates of our experiments. Specifically, our models do not predict the exact time or exact location of failure. In experiments with pure FG sand, surface eruptions nucleated at the location of greatest overpressure gradient, downslope of the model FS$<$1 boundary. We anticipate that this is a result of our models being homogeneous and isotropic, whereas the flume experiments have heterogeneity based on set-up and small variations in grain size and sorting. These heterogeneities will affect the permeability distribution and thus the pressure and instability distributions. More advanced models with stochastic heterogeneities could be developed to explore the importance of heterogeneity in localization of failure. We did not, however, address that issue as this research was focused on characterizing physical experiments and developing models that link the physical processes with the observed behaviour.

Our laboratory and experimental results show that for a fixed stratigraphic geometry composed of high-permeability pebbles overlain by sand–clay mixtures (up to 5% clay) the permeability, cohesion and failure angle influence the onset of failure and the type of failure. As clay content and cohesion increase and permeability decreases, we observe

Downloaded from http://sp.lyellcollection.org/ by guest on March 27, 2020

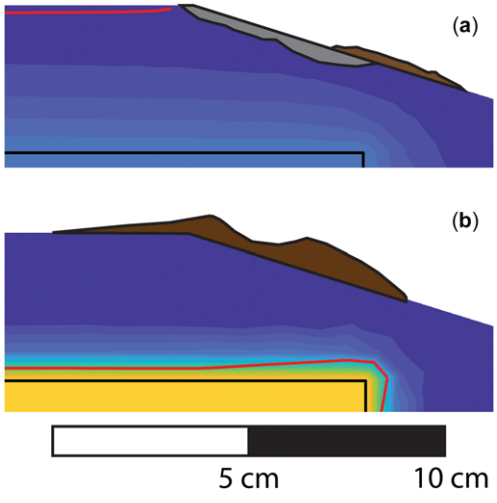

Fig. 5. Example results from numerical model of fluid flow and slope stability analysis from Figure 4 expanded and overlain with observed slope mass loss (in grey) or deposition (in brown) for (**a**) 100% FG sand experiment 4 and (**b**) 4% clay experiment 3. There is no vertical exaggeration.

that higher overpressure is required to induce failure and that failure transitions from surface eruption (100% FG sand) to surface eruption plus fissures, tension cracks and suspension of clay particles (2–5% clay). Our models of the physical experiments based on measured permeability, geometry and known boundary heads successfully predict the location of failures and the timing of failures to the zeroth order (e.g. Fig. 5). Combined, this documents a necessity to understand *in situ* properties to better understand the potential for failure location and type. Our modelling results, however, show that the geometry of the pebble layer and the overlying sand–clay mixtures influence the distribution of overpressure, which in turn affects the localization of failure. This result will motivate future studies on the influence stratigraphic architecture has on overpressure distribution and failure localization.

Conclusions

Submarine slope failures pose risks to coastal communities because of their ability to damage infrastructure and generate tsunamis. Slope failures on passive margins represent some of the largest mass failures on Earth, yet little is known about their dynamics. While numerous studies characterize slope failure deposits in terms of lithology, structure, seismic attributes and geometry, we lack direct observations of slope failure initiation and evolution. As a result, there is limited insight into the relationships between initial conditions, preconditioning, slope failure initiation and slope failure evolution.

We performed a suite of physical experiments in a benchtop flume to investigate submarine slope failure dynamics in relation to initial conditions, and numerical models were developed to quantify the observed processes. Submarine slope failures were induced under controlled pore pressure with varied mixtures of sand and clay (0–5 wt% clay) constrained to a constant pre-failure slope geometry.

Increased clay concentrations were observed to directly relate to an increase in pore pressure required to induce slope failure, attributed to clay particle cohesion and decreased hydraulic conductivity. Formation of elongated subsurface cavities along the flume–wall interface and surficial tensile cracking was only observed in experiments containing clays, indicating the importance of the presence of clay in their formation. No slump/block failure was observed in experiments. Insufficient clay content and a slow rate of pore pressure increase are considered to be the causes. Numerical models of our physical experiments using measured hydraulic properties are effective at simulating the distribution of overpressure and locations of potential failure for both cohesive and non-cohesive sediments and modes of failure. The model results demonstrate the importance clay has for permeability and cohesion, which helps define where failure conditions exist and when they occur. The correlation between the experiments and models gives strength to the interrogation of processes that models provide, and suggests that the upscaling of these models to natural systems can be effective at evaluating the potential for failure location and mode for known geometries and pressure sources.

Acknowledgements This research benefited from discussions with C. Paola and A. Abeyta. Comments by D. Sawyer and one anonymous reviewer helped improve the structure and content of the manuscript. Please contact the authors for original data and/or digital model results.

Funding This research was supported by the National Science Foundation (grant NSF-OCE 1753680 to BD).

Author contributions **MMWS**: formal analysis (equal), investigation (equal), methodology (supporting), software (equal), visualization (equal), writing – original draft (lead), writing – review & editing (equal); **BD**: conceptualization (lead), formal analysis (equal), funding acquisition (lead), investigation (equal), methodology (lead), project administration (lead), resources (lead), software (equal), supervision (lead), validation (lead), visualization (equal), writing – original draft (supporting), writing – review & editing (equal).

Downloaded from http://sp.lyellcollection.org/ by guest on March 27, 2020

References

Berthila, E.V.P., Badillo, E.J., Rodríguez, A.R. and ASTM D5084-10. 2010. *Standard Test Methods for Measurement of Hydraulic Conductivity of Saturated Porous Materials Using a Flexible Wall Permeameter*. ASTM International, West Conshohocken, PA, https://doi.org/10.1520/D5084-10

ten Brink, U.S., Chaytor, J.D., Geist, E.L., Brothers, D.S. and Andrews, B.D. 2014. Assessment of tsunami hazard to the U.S. Atlantic margin. *Marine Geology*, **353**, 31–54, https://doi.org/10.1016/j.margeo.2014.02.011

ten Brink, U.S., Andrews, B.D. and Miller, N.C. 2016. Seismicity and sedimentation rate effects on submarine slope stability. *Geology*, **44**, 563–566, https://doi.org/10.1130/G37866.1

Dan, G., Sultan, N., Cattaneo, A., Everchère, J.D. and Yelles, K. 2010. Mass-transport deposits on the Algerian margin (Algiers area): morphology, lithology and sedimentary processes. *In*: Mosher, D.C. *et al*. (eds) *Submarine Mass Movements and Their Consequences*. Advances in Natural and Technological Hazards Research, **28**. Springer, 527–539, https://doi.org/10.1007/978-90-481-3071-9_43

Fetter, C.W. 2001. Chapter 3: Properties of Aquifers. *Applied Hydrogeology*, 4th edn. Prentice Hall, Upper Saddle River, NJ.

Fine, I.V., Rabinovich, A.B., Bornhold, B.D., Thomson, R.E. and Kulikov, E.A. 2005. The Grand Banks landslide-generated tsunami of November 18, 1929: preliminary analysis and numerical modeling. *Marine Geology*, **215**, 45–57, https://doi.org/10.1016/j.margeo.2004.11.007

Fritz, H.M., Kongko, W. *et al*. 2007. Extreme runup from the 17 July 2006 Java tsunami. *Geophysical Research Letters*, **34**, L12602, https://doi.org/10.1029/2007GL029404

Gazioğlu, C., Yücel, Z.Y. and Doğan, E. 2005. Morphological features of major submarine landslides of Marmara Sea using multibeam data. *Journal of Coastal Research*, **214**, 664–673, https://doi.org/10.2112/03-0060.1

Hühnerbach, V. and Masson, D.G. 2004. Landslides in the North Atlantic and its adjacent seas: an analysis of their morphology, setting and behaviour. *Marine Geology*, **213**, 343–362, https://doi.org/10.1016/j.margeo.2004.10.013

Idarraga-García, J. and Vargas, C.A. 2013. Morphological expression of submarine landslides in the accretionary prism of the Caribbean continental margin of Colombia. *In*: Krastel, S. *et al*. (eds) *Submarine Mass Movements and Their Consequences*. Advances in Natural and Technological Hazards Research, **37**. Springer, 391–401, https://doi.org/10.1007/978-3-319-00972-8_35

Locat, J., ten Brink, U.S. and Chaytor, J.D. 2010. The Block composite submarine landslide, Southern New England slope, U.S.A.: a morphological analysis. *In*: Mosher, D.C. *et al*. (eds) *Submarine Mass Movements and Their Consequences*. Advances in Natural and Technological Hazards Research, **28**. Springer, 267–277, https://doi.org/10.1007/978-90-481-3071-9_22

Lucchi, R.G., Pedrosa, M.T., Camerlenghi, A., Urgeles, R., De Mol, B. and Rebesco, M. 2012. Recent submarine landslides on the continental slope of Storfjorden and Kveithola Trough-Mouth Fans (North West Barents Sea). *In*: Yamada, Y. *et al*. (eds) *Submarine Mass Movements and Their Consequences*. Advances in Natural and Technological Hazards Research, **31**. Springer, 735–745, https://doi.org/10.1007/978-94-007-2162-3_65

McAdoo, B.G., Pratson, L.F. and Orange, D.L. 2000. Submarine landslide geomorphology, US continental slope. *Marine Geology*, **169**, 103–136, https://doi.org/10.1016/S0025-3227(00)00050-5

Muhari, A., Imamura, F., Arikawa, T., Hakim, A.R. and Afriyanto, B. 2018. Solving the puzzle of the September 2018 Palu, Indonesia, tsunami mystery: clues from the tsunami waveform and the initial field survey data. *Journal of Disaster Research*, **13**, sc20181108, https://doi.org/10.20965/jdr.2018.sc20181108

Sawyer, D.E. and Devore, J.R. 2015. Elevated shear strength of sediments on active margins: evidence for seismic strengthening. *Geophysical Research Letters*, **42**, 10216–10221, https://doi.org/10.1002/2015GL066603

Sawyer, D.E., Flemings, P.B., Buttles, J. and Mohrig, D. 2012. Mudflow transport behavior and deposit morphology: role of shear stress to yield strength ratio in subaqueous experiments. *Marine Geology*, **307–310**, 28–39, https://doi.org/10.1016/j.margeo.2012.01.009

Shipley, T.H., Stoffa, P.L. and Dean, D.F. 1990. Underthrust sediments, fluid migration paths, and mud volcanoes associated with the accretionary wedge off Costa Rica: Middle America Trench. *Journal of Geophysical Research*, **95**, 8743–8752, https://doi.org/10.1029/JB095iB06p08743

Terzaghi, K., Peck, R.B. and Mesri, G. 1996. *Soil Mechanics in Engineering Practice*. Wiley, New York

Westbrook, G.K. and Smith, M.J. 1983. Long decollements and mud volcanoes: evidence from the Barbados Ridge Complex for the role of high pore-fluid pressure in the development of an accretionary complex. *Geology*, **11**, 279–283, https://doi.org/10.1130/0091-7613(1983)11<279:LDAMVE>2.0.CO;2